RSC Sustainability

ROYAL SOCIETY OF CHEMISTRY

PAPER

View Article Online
View Journal | View Issue

Cite this: *RSC Sustainability*, 2025, **3**, 5571

Low-capacitance pulsed discharge enables heat- and solvent-free delamination of lithium-ion battery cathodes

Chiharu Tokoro, *[ab] Moe Nakahara, [a] Takatoshi Kurihara, [a] Akiko Kubota, [a] Mauricio Córdova-Udaeta, [a] Asako Narita [a] and Yutaro Takaya [b]

Recovering cathode-active materials (CAMs) from end-of-life lithium-ion batteries without added heat or chemicals is pivotal for low-impact, closed-loop manufacturing. We show that circuit capacitance dictates whether a single electrical pulse yields clean, solvent-free delamination or destructive pulverization. Commercial $Li(Ni_{0.33}Mn_{0.33}Co_{0.33})O_2$ coated on aluminum foil was exposed to 375–475 J discharges from 6.4 μF (low-C) and 400 μF (high-C) capacitor banks. The low-C circuit squeezed the stored energy into sub-200 μs current spikes (≈15 kA) that heated the CAM/Al interface from ambient to ≈500 K within 100 μs, generating transient stresses of tens of MPa before the foil was severed. A 425 J pulse cleanly lifted the entire coating (99.9 wt% CAMs), leaving only 0.3 wt% residual aluminum, and X-ray diffraction confirmed that the layered oxide structure remained intact. Conversely, the high-C circuit stretched the same energy over > 500 μs, diverting the current into the plasma and fragmenting both the foil and coating. The delamination plateaued near 90 wt%, and at 475 J, aluminum contamination surged nine-fold. One-dimensional transient heat-rise analysis corroborated that temporal energy concentration—enabled by low capacitance—triggers the instantaneous interfacial heating required for clean separation, whereas energy dispersion channels power into fragmentation. This heat- and solvent-free pre-treatment supplies battery-grade layered oxides ready for direct cathode recycling, eliminating the furnaces, acids, and wastewater typical of pyro- or hydrometallurgical routes.

Received 26th April 2025
Accepted 4th October 2025

DOI: 10.1039/d5su00304k

rsc.li/rscsus

Sustainability spotlight

Conventional cathode delamination relies on furnaces and leachants that generate CO_2 and effluents. Our low-capacitance single-pulse discharge cleanly detaches $Li(Ni_{0.33}Mn_{0.33}Co_{0.33})O_2$ from aluminum in <100 μs, recovering 99.9 wt% CAMs with just 0.2 wt% aluminum contamination—no heat, solvents, or reagents required. The oxide remains chemically intact, enabling the direct recycling of CAMs in new batteries, bypassing energy-intensive pyro- or hydrometallurgy processes. Prospective LCA shows that this delamination pass can reduce process energy by 74% and boost CAM yield by 1.5-fold compared to commercial pyrometallurgy. Previously, our pulse delamination plateaued at 95% recovery and 3% aluminum contamination; capacitance control breaks this barrier, delivering a realistic, low-energy pre-treatment that advances SDGs 7 and 12.

Introduction

Lithium-ion batteries (LiBs) are extensively used in electric vehicles (EVs), portable electronics, and aerospace applications owing to their high energy density and excellent cycling stability.[1–3] The global shift toward carbon neutrality and advancements in battery technology have accelerated EV adoption, with worldwide sales increasing from 760 000 units in 2016 to 13.8 million units in 2023.[4,5] This rapid expansion is expected to generate a substantial volume of LiB waste in the coming decades.[6–8]

LiBs contain valuable metals such as lithium (Li), cobalt (Co), and nickel (Ni) in their cathode active materials (CAMs), most of which are sourced from geographically concentrated regions.[9–12] The growing demand has raised concerns over resource depletion, supply chain vulnerabilities, and environmental impacts associated with improper disposal.[13] In response, regulatory frameworks, such as the European Union's battery regulations, mandate the recovery of key metals and set recycling targets to promote a circular economy for LiBs.[14]

Current recycling practices predominantly rely on pyrometallurgical processes operating at temperatures above 1100 °C (ref. 15–17) and hydrometallurgical methods involving acid leaching and solvent extraction.[18–24] These methods focus on

[a]*Faculty of Science and Engineering, Waseda University, 3-4-1 Okubo, Shinjuku-ku, Tokyo 169-8555, Japan. E-mail: tokoro@waseda.jp*

[b]*Faculty of Engineering, The University of Tokyo, 7-3-1 Hongo, Bunkyo-ku, Tokyo 113-8656, Japan*

recovering Li as carbonates and Co and Ni as sulfates with high purity, enabling their recycling for battery production. However, they also require high costs, substantial energy input, and impose environmental burdens through CO_2 emissions and the generation of wastewater effluents.

Recently, hybrid and direct recycling approaches have been proposed to recover Co and Ni as oxides without passing through conventional pyrometallurgical or hydrometallurgical processes, thereby enabling regeneration through annealing.[25–28] These methods aim to reduce heat input, chemical consumption, and overall energy demand compared with conventional processes. For direct recycling, preserving the crystal structure of CAMs is essential. Various hydrometallurgical approaches have been investigated to achieve this goal;[29–34] however, the lack of efficient and selective physical delamination techniques remains a major challenge in this regard.[35] Investigations into methods such as thermal decomposition, solvent-assisted separation, ultrasonic cleaning, mechanical grinding, and sieving have been conducted.[36–39] Nevertheless, no definitive or robust method for consistently achieving high-purity physical separation has been established.

We recently proposed an electrical pulsed discharge method for separating CAMs from an aluminum (Al) foil without using heat, solvents, or chemical reagents. A single electrical pulse induces a high current flow in the Al foil, generating localized Joule heating that weakens the adhesion and enables precise delamination.[40] The separated CAMs retain their chemical and electrochemical properties, and the scalability and applicability of this method in air and water environments have been demonstrated.[41–43] Moreover, this method is applicable not only to cathode sheets but also to anode sheets and $LiFePO_4$ cathodes.[44] Because this phenomenon occurs within a few hundred microseconds, the energy required for delamination is significantly lower than that of heating-based methods. According to our previous life cycle assessment (LCA), implementing electrical pulsed discharge for direct recycling could reduce energy consumption to 75% of that required by conventional pyrometallurgical processes, while increasing the value of recovered CAMs by approximately 1.5 times in terms of manufacturing energy savings.[45] However, our previous studies indicated that the delamination rate was limited to approximately 95%, and the recovered CAMs contained approximately 3 wt% Al contamination.[40] Furthermore, the diversity of battery designs and aging-induced degradation complicate the achievement of stable, high-purity separation.[46,47] Thus, consistently exceeding a 95% delamination rate, as required by the EU battery regulation proposal, remains a significant challenge.

In this study, we systematically investigated the influence of circuit capacitance on the delamination behavior during electrical pulsed discharge, aiming to improve the delamination efficiency and minimize Al contamination. Although the total energy was maintained constant, the difference in capacitance affected the voltage–current profile and discharge duration, leading to distinct separation outcomes. The energy imparted by electrical pulsed discharge is distributed between Joule heating, which facilitates adhesion weakening, and expansion or destruction *via* vaporization and plasma formation, respectively. The voltage–current characteristics strongly influence the energy distribution. To achieve high-precision delamination, it is critical to allocate energy predominantly to Joule heating while restricting plasma formation to the adhesive interface and preventing the vaporization or pulverization of the CAMs and Al layers. By comparing two discharge circuits with different capacitances under controlled conditions, we identified the critical electrical parameters required to achieve high-efficiency delamination, thereby contributing to the development of robust direct recycling processes aligned with emerging regulatory standards.

Experimental

LiB cathode sheet samples

Spent laminated LiBs from EVs were discharged and disassembled to extract the cathode sheets for the experiments. The structure of the disassembled battery is shown in Fig. 1(a). The extracted cathode sheets were washed with diethyl carbonate to remove the residual electrolyte, dried, and stored in a sealed stainless steel container. The state of health (SOH) of the battery before disassembly, which represents the remaining capacity relative to the initial capacity, was 71%. Fig. 1(b) shows a top-view photograph of the cathode sample, and Fig. 1(c) shows its cross-section. The cathode sheet was cut into specimens with a width of 25 mm and length of 130 mm for use in the experiments. It consisted of an Al current collector (thickness: 15 μm) coated on both sides with a 60 μm-thick cathode active material (CAM) layer. The CAM layer comprised lithium nickel manganese cobalt oxide ($Li(NixMnyCoz)O_2$) as the active material, polyvinylidene fluoride (PVDF) as the binder, and carbon black as a conductive additive.

Electrical pulsed discharge circuit

Electrical pulsed discharge experiments were conducted using circuits A and B, which had different capacitances. The circuit diagrams of circuits A and B are shown in Fig. 2(a) and (b),

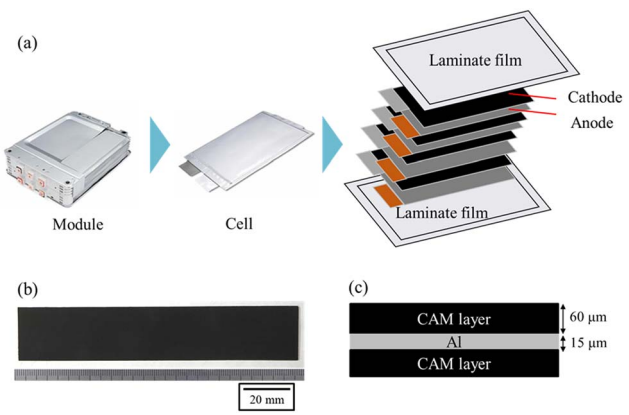

Fig. 1 Schematic of LiB cathode sheet sample. (a) Structure of the laminated LiB, (b) top view of the extracted cathode sheet, and (c) cross-sectional schematic of the cathode sheet.

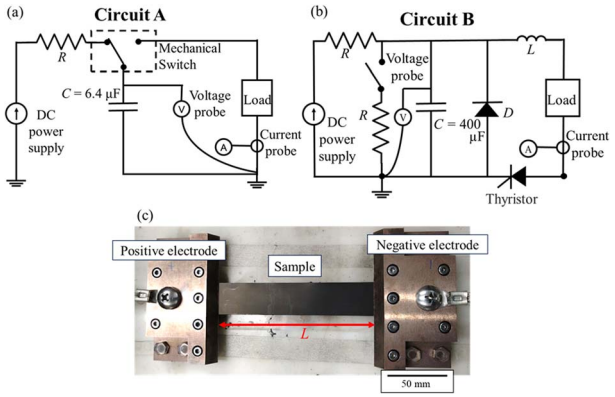

Fig. 2 Experimental setup: (a) circuit diagram of circuit A, (b) circuit diagram of circuit B, and (c) configuration of the load section with the LiB cathode sheet sample.

respectively. Both circuits consisted of charging and discharging circuits.

In circuit A shown in Fig. 2(a), eight capacitors with a rated capacitance of 0.8 μF (FLAAA, Shizui Electric Co., Inc., Hyogo, Japan) were connected in parallel to the charging circuit. A DC power supply with a maximum output voltage of 40 kV (152A-40 kV-POS, TDK-Lambda Corp., Tokyo, Japan) was used to charge the capacitor. A 1 kΩ resistor was connected between the power supply and capacitors to prevent reverse current flow into the DC power supply. The charging voltage was controlled using a pulse power controller (Tanacom Corp., Kumamoto, Japan) connected to a mechanical switch (E60-DT-80-1-15-BD, Ross Engineering Corp., California, USA) and a DC power supply. Once the capacitors were fully charged, the mechanical switch was activated to connect the discharge circuit, releasing the stored energy into the load.

In circuit B, as shown in Fig. 2(b), two capacitors with rated capacitances of 200 μF were connected in parallel to the charging circuit. A DC power supply with a maximum output voltage of 4.3 kV (FB-321A; Ushio Inc., Tokyo, Japan) was used to charge the capacitors. A resistor was connected between the power supply and capacitors to prevent reverse current flow into the DC power supply. Once the capacitors were fully charged, a thyristor with a rated voltage of 4.4 kV and a rated current of 40 kA (Infineon Technologies, Augsburg, Germany) was triggered by applying a gate current, switching the circuit to discharge mode, and transferring the stored energy to the load.

The LiB cathode material sample was placed in the load section, as shown in Fig. 2. Fig. 2(c) shows a top-view image of the LiB cathode material. The sample was clamped at both ends using copper-tungsten electrodes, and 5 mm of each end was held. The distance between the electrodes, L, was set to 120 mm for a sample length of 130 mm. The electrodes and sample were placed inside a stainless steel (SUS) chamber, and the lid was closed to prevent sample scattering during the electrical pulsed discharge test. Furthermore, electrical pulsed discharge tests were conducted in a shielded room to minimize the influence of electromagnetic noise on the measurements of the electrical characteristics.

The voltage and current data during the pulsed discharge were obtained using a voltage probe (HV-P60A, Iwatsu Electric Co., Ltd, Tokyo, Japan) and a current probe (CURRENT MONITOR MODEL 110A, Pearson Electronics, Inc., California, USA) connected to a digital oscilloscope (HDO4104A, Teledyne Japan Corp., Tokyo, Japan).

Electrical pulsed discharge experiment

In this study, the charging energies were set to 375, 425, and 475 J. Considering the total capacitance of each circuit, the corresponding charging voltages were adjusted to 10.8, 11.5, and 12.2 kV for circuit A (6.4 μF), and 1.37, 1.46, and 1.54 kV for circuit B (400 μF), respectively.

High-speed imaging was performed using the shadowgraph method to investigate the delamination mechanisms of CAMs from the Al foil. The visualization system consisted of a pulsed laser light source (Cavilux Smart, Cavitar Ltd, Tampere, Finland), a pair of plano-convex lenses, and a high-speed video camera (HPV-X2, Shimadzu Corp., Kyoto, Japan), which operated at 1.0×10^6 frames per s with an exposure time of 200 ns. The camera was triggered when the detected discharge current exceeded 1 kA. Owing to the positional constraints between the experimental setup and circuit A, high-speed imaging was feasible only for circuit A with a capacitance of 6.4 μF, whereas imaging for circuit B was not possible under the current experimental setup.

The current and voltage waveforms obtained during the experiments were used to analyze the temperature distribution in the sample during the electrical pulsed discharge. The analysis was conducted using COMSOL Multiphysics, a general-purpose simulation software based on the finite element method, which specifically utilizes its AC/DC module. Table 1 lists the material properties employed in the thermal and stress analyses.[47–51]

Powder and chemical analysis

After the electrical pulsed discharge experiments, the delaminated particles were collected and subjected to particle size distribution analysis, Al concentration measurements, and X-ray diffraction (XRD) analysis. The particle size distribution was determined by sieving the collected particles using mesh sizes of 300 μm, 600 μm, 1.18 mm, 2.36 mm, 4.75 mm, and 9.5 mm. Sieving was performed manually to minimize the damage to foil-like particles. The crystal phases of the powders were identified by XRD (SmartLab, Rigaku Corp., Tokyo, Japan) using

Table 1 Material properties used for thermal and stress analyses

Properties	Al foil	CAMs	Air
Density [kg m^{-3}]	2700	3450	1.18
Specific heat [J (kg^{-1} K^{-1})]	900	830	1007
Thermal cond. [W (m^{-1} K^{-1})]	238	0.78	0.0262
Relative permittivity [—]	1.00	25.0	—
Conductivity [S m^{-1}]	4.99×10^7	0.523	—
Young's modulus [GPa]	—	1.44	—
Poisson's ratio [—]	—	0.305	—

SmartLab Studio software and the ICDD PDF-2 Release 2020 RDB database.

The recovered CAM particles were dried, pulverized using an agate mortar, and digested in aqua regia ($HCl : HNO_3 = 1 : 1$) at 180 °C for 3 h in a sealed Teflon vessel. After cooling, the solutions were diluted with ultrapure water, filtered through a 0.45 μm membrane, and analyzed using ICP-OES (iCAP6500-Duo, Thermo Fisher Scientific, MA, USA). Calibration was performed for Al at an analytical wavelength of 308.215 nm, which showed better fitting and consistency with the standard solutions compared to 396.152 nm (Table S1 and Fig. S1).

Results and discussion

Observation of CAM delamination and pulverization

Photographs of the cathode samples after pulsed discharge are presented in Fig. 3. Fig. 3(a) shows the samples obtained from circuit A. At a charging energy of 375 J, the CAMs layer remained adhered to the Al foil, indicating that the energy was insufficient for delamination. However, at 425 and 475 J, the CAMs layer was entirely separated from the Al foil interface. The delamination and recovery rates of the CAMs layer were 0.64 wt% at 375 J, 99.9 wt% at 425 J, and 98.3 wt% at 475 J.

At 425 J, the recovered Al foil retained its original, sheet-like structure. In contrast, at 475 J, the Al foil exhibited pronounced wrinkles and multiple-fracture lines. These morphological changes at 475 J suggest that the Al foil experienced significant mechanical damage, likely caused by the enhanced plasma expansion and associated shock forces during high-energy discharge.

Fig. 3(b) shows photographs of the cathode samples after pulsed discharge using circuit B. At 375 J, the CAMs layer remained adhered to the Al foil, similar to the results obtained for circuit A. However, at 425 J, delamination of the CAMs layer was observed, and the recovery rate of the CAMs layer was 11.2 wt% at 375 J and 90.3 wt% at 425 J.

Unlike circuit A, at 425 J, a significant portion of the Al foil disintegrated into fine particles, contaminating the recovered CAMs layer. At 475 J, the input energy exceeded the threshold required for CAM delamination, leading to CAM delamination and extensive Al fragmentation and pulverization, thereby complicating manual recovery. The pulverization of the delaminated Al foil and CAM layer hinders their subsequent physical separation, such as sieving, gravity separation, and eddy current separation, making them undesirable for advanced recycling processes.

Thus, although the precise delamination of the Al foil and CAMs layer *via* electrical pulsed discharge is achievable with an appropriate energy input, the delamination behavior differs depending on the capacitance value. Circuit A (6.4 μF) enabled more precise delamination compared to circuit B (400 μF).

Observation of electrical pulsed discharge

The behavior of the electrical pulsed discharge was observed using high-speed imaging and voltage/current waveform

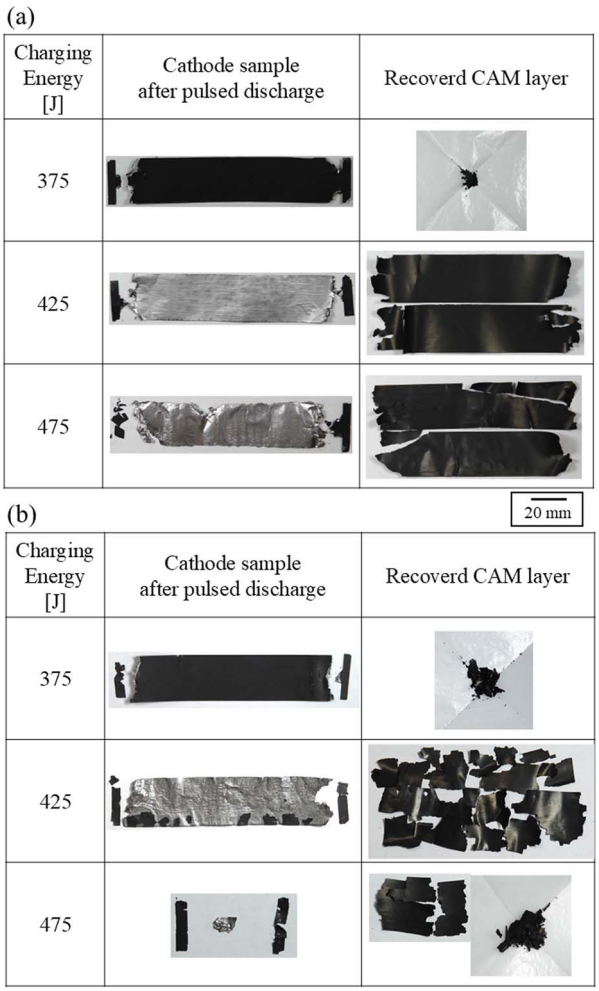

Fig. 3 Delamination behavior of the Al foil and CAMs layer after electrical pulsed discharge: (a) circuit A, (b) circuit B.

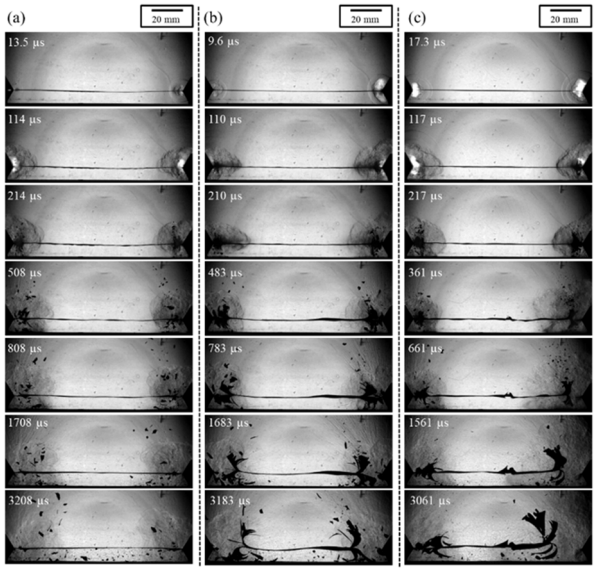

Fig. 4 High-speed imaging of the electrical pulsed discharge in circuit A at (a) 375, (b) 425, and (c) 475 J.

analysis. High-speed imaging was obtained only for circuit A (Fig. 4), whereas the voltage and current waveforms were recorded for circuits A (Fig. 5(a)) and B (Fig. 5(b)).

When a high-voltage pulse was applied, plasma formation was immediately detected at both electrode contact points, followed by rapid gas expansion owing to Joule heating (Fig. 4). A slight voltage drop and current increase were observed immediately after the pulse, as shown in Fig. 5(a), confirming that dielectric breakdown occurred at this stage. This expansion wave, whose magnitude was confirmed from the image, is one of the driving forces for the delamination of the CAMs layer from the Al foil. However, because the magnitude of the expansion wave at 375 J (where delamination did not occur) was not significantly different from that at higher energies, it was inferred that the driving force for delamination also strongly depends on other factors, such as the temperature generated at the interface.

Our previous study confirmed that the delamination of the CAMs layer from the Al foil *via* electrical pulsed discharge is driven by both the expansion wave and Joule heating caused by the high current flowing through the Al foil.[46,47] The temperature increase causes deactivation of the adhesive at the interface, while the resulting temperature gradient across the CAMs layer generates thermal stress.

Although high-speed imaging was not obtained for circuit B under the current experimental setup, Fig. 5(b) illustrates a more pronounced voltage drop and current increase immediately after pulse application compared with circuit A. Thus, dielectric breakdown occurred earlier in the high-resistance region between the electrodes and the sample, triggering the generation of an expansion wave and the melting or severing of the Al foil. In contrast to circuit A, multiple small voltage drops and current increases were observed throughout the conduction period in circuit B, suggesting that the current path became more distributed owing to conduction through ionized materials in the surrounding plasma. Consequently, the current flowing through the Al foil was reduced, suppressing the Joule heating and thermal stress required for the delamination. Therefore, circuit B failed to achieve delamination despite having the same energy input as circuit A (Fig. 3).

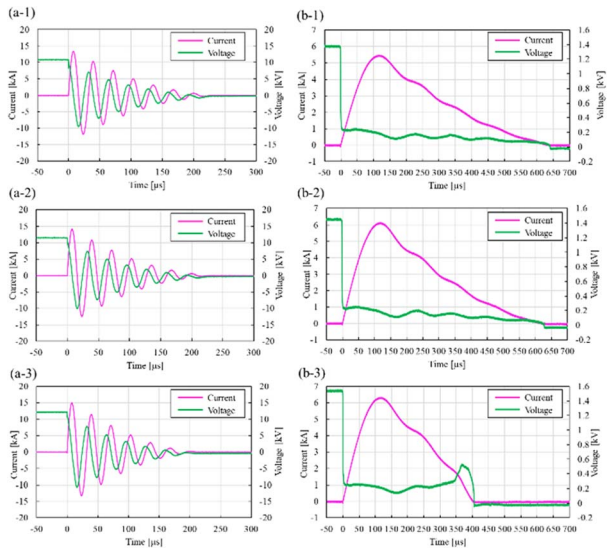

Fig. 5 Voltage and current waveforms during electrical pulsed discharge: (a-1) 375 J, (a-2) 425 J, and (a-3) 475 J in circuit A, and (b-1) 375 J, (b-2) 425 J, and (b-3) 475 J in circuit B.

Properties of delaminated CAMs particles

As shown in Fig. 6(a), most of the delaminated particles obtained using circuit A (6.4 μF) were larger than 9.5 mm. In contrast, the cumulative distribution for circuit B (400 μF) shifted toward smaller particle sizes, indicating a higher proportion of small fragments in this circuit than in circuit A. As shown in Fig. 6(b), the concentration of Al contamination in the delaminated CAMs was higher for circuit B than for circuit A. For circuit B, the sample treated at 475 J resulted in finer particles and higher Al contamination than that treated at 425 J. The raw ICP-OES and XRF data for all conditions are summarized in Table S2 and Fig. S2. These results confirm that the input energy was more efficiently utilized for delamination in circuit A. In contrast, in circuit B, a portion of the energy was consumed for plasma formation and the pulverization of the CAMs and Al foil.

The XRD patterns of the delaminated particles are presented in Fig. 7(a). All the diffraction peaks matched the standard pattern of NCM333 ($Li(Ni_{0.33}Co_{0.33}Mn_{0.33})O_2$), corresponding to the Powder Diffraction File (PDF) card no. 01-083-7585. This confirms that, under all the tested conditions, the CAMs were delaminated without undergoing chemical degradation. In contrast, a closer examination of the peak intensities of the most intense diffraction peak revealed that the sample treated at 425 J with 6.4 μF (circuit A) exhibited the highest intensity, whereas the sample treated at 475 J with 400 μF (circuit B) exhibited the lowest.

Because no distinct amorphous halo was observed, Rietveld refinement was not possible. Instead, a Reference Intensity Ratio (RIR) analysis was performed assuming two crystalline phases: NCM333 (PDF No. 01-083-7585) and graphite (PDF No. 00-056-0160). The relative contribution of the NCM333 phase remained consistently high across all tested conditions (96.8–98.4%), and no peak shift or broadening was detected, indicating that significant degradation of the crystallinity did not occur. SEM images (Fig. 7(c) and (d)) further confirmed that fracture occurred only at the agglomerate level, and no

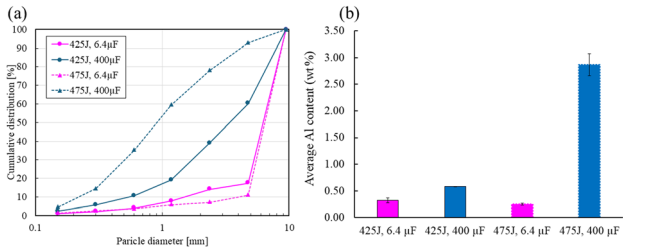

Fig. 6 Cumulative particle size distribution (a) and residual Al concentration determined by ICP-OES (b) of delaminated CAMs particles obtained under different discharge conditions.

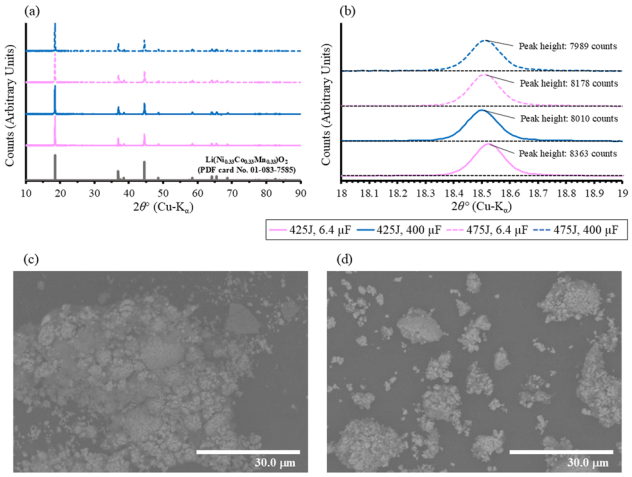

Fig. 7 XRD patterns (a), magnified views of the most intense diffraction peaks (b), and SEM images of the delaminated particles at 6.4 μF, 425 J (c) and 400 μF, 475 J (d).

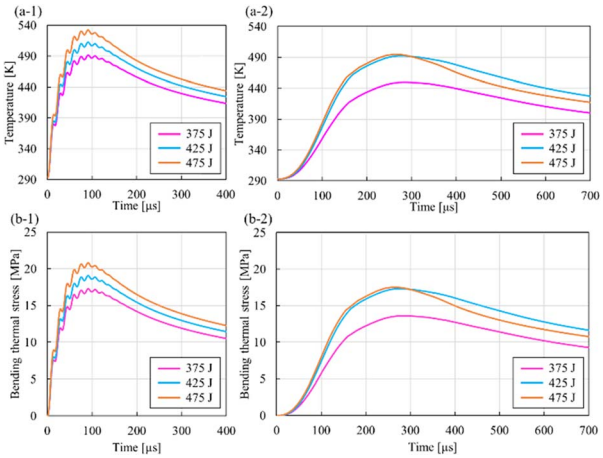

Fig. 8 Temperature evolution at the Al/CAM interface in (a-1) circuit A and (a-2) circuit B; thermal stress in the CAM layer under different input energy conditions in (b-1) circuit A and (b-2) circuit B.

destruction of individual CAM particles was observed in the agglomerates. Therefore, the lower peak intensity observed under circuit B is more plausibly attributed to secondary factors, such as the surface attachment of impurities or slight variations in the particle size distribution rather than intrinsic structural changes.

These results collectively demonstrate that, under the condition of 425 J in circuit A, an exceptionally clean and precise separation was achieved, with a delamination rate of 99.9% (Fig. 3(a))and Al contamination suppressed to below 0.3 wt% (Fig. 6(b)). Moreover, the recovered CAMs exhibited negligible changes in their chemical structure and crystallinity (Fig. 7(a)), confirming the high integrity of the delaminated materials. These results suggest that pulsed electric field-assisted delamination is a more favorable method for enabling the direct recycling of CAMs than conventional approaches involving thermal treatment or chemical additives.

Estimation of Joule heating and thermal stress

Fig. 8(a) illustrates the temperature evolution at the Al/CAM interface for circuits A (a-1) and B (a-2) under different input energy conditions. Because this temperature estimation did not account for heat dissipation, the temperature values on the vertical axis were relatively high. It was also assumed that all the current flowed through the Al foil.

The temperature rapidly increased after the electrical pulsed discharge and reached a peak before decreasing gradually. Compared with circuit B, circuit A generally exhibited a higher temperature increase. This indicates that a larger proportion of the input energy in circuit A was allocated to Joule heating owing to the higher current flow, even with the same total energy input.

As shown in Fig. 3, delamination of the Al foil and CAM layer did not occur at 375 J in either circuit. This suggests that delamination requires the degradation of the adhesive layer (represented by PVDF) once a certain level of heat generation is exceeded. Based on the temperature estimation, Joule heating that raises the interface temperature above 490 K is presumed necessary to weaken the adhesive bond and facilitate delamination. In particular, $LiPF_6$, a commonly used electrolyte salt, is known to thermally and hydrolytically decompose into PF_5 and HF, even in the presence of trace amounts of water, with HF formation reported to occur at temperatures ranging from 433 to 543 K.[52–54] The generated HF can chemically attack polyvinylidene fluoride (PVDF), the binder material, leading to chain scission and loss of adhesion strength.[55–57] This chemical degradation, coupled with the thermal softening of PVDF at elevated temperatures, significantly weakens the interface and promotes CAMs delamination.

Fig. 9 shows the results of differential scanning calorimetry (DSC) and gel permeation chromatography (GPC) analyses conducted to evaluate the thermal and molecular characteristics of PVDF, respectively. The DSC thermograms comparing reagent-grade PVDF with CAM-bound PVDF revealed an endothermic melting peak at 431 K for reagent-grade PVDF and 445 K for CAM-bound PVDF, indicating that the PVDF used in the samples in this study exhibited a slightly higher melting point owing to its composite nature and potentially higher crystallinity. However, the onset of thermal decomposition occurred at a lower temperature for CAM-bound PVDF than for the pure reagent, suggesting that residual electrolyte species and conductive additives reduce the overall thermal stability. These

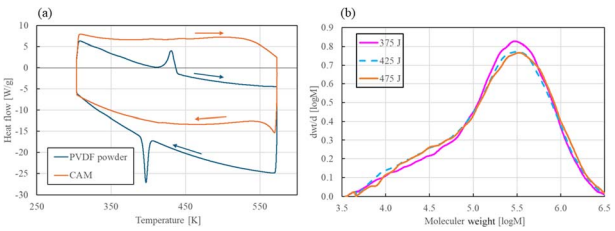

Fig. 9 DSC thermograms of reagent-grade PVDF and CAM-bound PVDF (a) and GPC chromatograms of PVDF after pulsed discharge (b).

results indicate that interfacial temperatures exceeding 445 K are sufficient to induce the thermal softening of the PVDF binder. According to literature reports,[55–57] HF generated from electrolyte decomposition in this temperature range may chemically degrade the PVDF. Such chemical degradation, together with thermal softening, can further reduce the adhesive strength and promote CAMs delamination.

The GPC analysis showed negligible differences in the molecular weight distribution of PVDF extracted from the samples after electrical pulsed discharge in circuit B, demonstrating that significant bulk PVDF degradation did not occur and that the chemical changes were confined to a highly localized region near the CAM/Al interface. Because GPC analysis was performed on samples from circuit B, where the differences in delamination behavior were the most pronounced, the absence of major differences further suggests that samples from circuit A, where reactions were milder, would exhibit similarly minimal changes.

At input energies of 425 J and higher, circuit A achieved a higher delamination rate than circuit B, which can be explained by the generally higher peak temperatures attained in circuit A. However, in circuit B, although the peak temperatures at 425 J and 475 J were nearly identical, the 475 J condition resulted in pulverization rather than delamination. This suggests that a portion of the input energy was consumed in fragmentation rather than delamination. This phenomenon cannot be explained by the temperature evolution alone. As previously discussed, it is inferred that in circuit B, part of the input energy was consumed for plasma formation and pulverization of both the CAMs and Al foil, thereby limiting the current flow through the Al foil compared with circuit A. This inference is supported by the finer particle sizes, higher Al contamination, and slightly reduced crystallinity of the CAMs, as shown in Fig. 6 and 7. In other words, local melting at the electrode grips caused an early loss of electrical contact; as the foil edges were severed, part of the current dispersed into the surrounding plasma, which reduced the effective Joule heating within the Al foil and kept the interface below the required adhesion-weakening threshold.

When the Al/CAM interface experiences a rapid temperature rise following an electrical pulsed discharge, a significant temperature gradient (ΔT) develops between the heated interface and the ambient air side, which remains at 25 °C. This temperature gradient induces thermal stress (σ), which can be expressed as,

$$\sigma = E_s/(1 - \nu) \times \Delta T, \quad (1)$$

where E represents Young's modulus, ν is Poisson's ratio, and a is the area. Fig. 8(b) shows the calculated thermal stress induced by the temperature gradient within the CAM layer under different input energy conditions using the material properties listed in Table 1. As expressed in eqn (1) The thermal stress is proportional to the temperature gradient across the CAM layer. Because the temperature gradient peaked when the maximum temperature was reached, Fig. 8(a) and (b) exhibit nearly identical trends. Moreover, because circuit A had a larger temperature gradient than circuit B, the resulting thermal stress was generally higher, leading to a greater tendency for delamination in circuit A.

Another important observation is the significant difference in the timing of peak thermal stress between circuits A and B. The maximum thermal stress occurred within 100 μs in circuit A, whereas it required more than 250 μs in circuit B. Although direct high-speed imaging could not be captured for circuit B, a plausible mechanism can be inferred as follows: upon pulse application, the Al foil at the electrode ends melted and was severed, causing the Al foil to gradually tear away from the electrodes. By 250 μs, the detached Al foil likely lost almost all electrical contact with the electrodes.

Consequently, in circuit A, a stable high current was maintained during the critical period when significant thermal stress developed, thereby ensuring consistent delamination. In contrast, in circuit B, substantial thermal stress did not develop until the electrical conduction to the Al foil was no longer sustained. In circuit B, increasing the input energy led to the pulverization of the cathode sheet before delamination could occur, explaining why higher energy did not result in successful delamination. Thus, the main effects of each circuit A summarized as follows: circuit A facilitates interfacial delamination by inducing focused Joule heating and thermal stress before structural damage occurs, whereas circuit B predominantly leads to mechanical fragmentation owing to delayed and dispersed energy input.

It should also be noted that in pulsed discharge systems, the discharge characteristics are governed not only by the capacitance but also by the total resistance of the circuit, which includes the wiring length, electrode geometry, and overall device scale. These factors, together with the resistance of the sample, form an LCR circuit that determines the current waveform and energy delivery profile. Although the two circuits in this study were implemented in different systems and could not be directly compared quantitatively, a clear relationship between capacitance and discharge duration was observed. This enables a qualitative understanding of how circuit design influences the timing and concentration of Joule heating and thermal stress, ultimately affecting the delamination behavior.

Conclusion

This study investigated the influence of capacitance on the delamination of cathode active materials (CAMs) from Al foils in lithium-ion battery (LiB) cathodes using electrical pulsed discharge. The high current generated during the pulsed discharge flowed through the Al foil, resulting in Joule heating that increased the temperature at the adhesion interface. This temperature increase induced adhesive degradation and created thermal stress owing to the temperature gradient, ultimately leading to delamination. However, variations in capacitance alter the energy distribution between voltage and current, significantly influencing the proportion of current flowing through the Al foil and, thus, the delamination efficiency.

For circuit A (6.4 μF), with a lower capacitance, the duration of the high current flow was less than 100 μs, enabling stable

current conduction through the Al foil before it melted and was severed, allowing effective delamination. As a result, a stable delamination rate exceeding 99% was achieved with an appropriate energy input. In contrast, in circuit B (400 μF), with a higher capacitance, the high current flow duration extended beyond 250 μs, during which the Al foil detached from the electrodes and the surrounding plasma developed. This reduction in the conductive path diverted the current away from the foil, leading to plasma expansion and increased mechanical fragmentation. Consequently, delamination became less efficient, and more pulverization occurred.

This trend was particularly evident at higher energy levels in circuit B, indicating that the capacitance affects the division of input energy between interfacial delamination and bulk fragmentation. In circuit B, the prolonged current flow and earlier severing of the Al foil disrupted the main conduction path, diverting the current into the surrounding space, where bright discharge emissions were visually observed. This coincided with the significant pulverization of the cathode active materials. This behavior is consistent with reports of plasma-induced fragmentation and interfacial damage under pulsed discharge conditions.[58,59] These findings underscore the importance of carefully tuning the discharge parameters to avoid excessive pulverization and maintain selective delamination. In essence, circuit A enabled a short and intense current pulse that focused the energy into Joule heating and thermal stress at the interface before electrode damage or plasma expansion occurred, thereby allowing clean and selective delamination. A smaller capacitance enables stable delamination by concentrating the input energy on interfacial separation.

Overall, low-capacitance pulsed discharge emerged as a promising technique for achieving a delamination rate exceeding 99% for a 25 mm × 130 mm cathode sheet, with Al contamination suppressed below 0.3 wt% and without inducing chemical degradation or loss of crystallinity in the recovered CAMs, thus meeting the EU battery regulation targets without the use of heat or chemicals. Importantly, these results also address key limitations identified in our previous LCA,[45] which was based on early experiments using 30 mm × 80 mm cathode sheets and reported a delamination efficiency of 93.9% with 2.95 wt% Al contamination.[40] That study highlighted the need for larger-area delamination and higher material purity to offset the environmental burden associated with equipment use. Specifically, although the environmental load of the electrical pulsed discharge equipment was relatively high, its operational environmental burden was low. The analysis concluded that enhancing the processing area and improving the purity in a single operation would significantly improve overall sustainability. These improvements contribute to reducing the environmental burden per functional unit and further support the feasibility of the industrial-scale implementation of the process.

Author contributions

C. T.: conceptualization, methodology, project administration, funding acquisition, resources, supervision, writing – review & editing. M. N.: investigation, data curation, writing – original draft. T. K.: validation, visualization. A. K.: formal analysis, validation. M. C.-U.: formal analysis, validation. A. N.: formal analysis, validation. Y. T.: formal analysis, validation.

Conflicts of interest

There are no conflicts to declare.

Data availability

All data supporting the findings of this study are included within the article.

The high-speed imaging data generated during the study (movies S1–S3, avi format) and ICP-OES/XRF analytical data of the Al concentrations (Tables S1/S2 and Fig. S1/S2) are available as Supplementary Information (SI). Supplementary information: it contains high-speed imaging videos (avi format) corresponding to the pulsed discharge experiments at 375 J, 425 J, and 475 J for the 6.4 μF circuit condition (movies S1–S3), as well as ICP-OES and XRF analytical data of Al concentrations under different discharge conditions (Tables S1/S2 and Fig. S1/S2). See DOI: **https://doi.org/10.1039/d5su00304k**.

Acknowledgements

Part of this work was performed as part of the activities of the Research Institute of the Sustainable Future Society, Waseda Research Institute for Science and Engineering, Waseda University. This research was supported by JSPS KAKENHI Grant Number 23K25037 (Scientific Research (B)).

References

1 K. Choubey, K.-S. Chung, M. Kim, J. Lee and R. R. Srivastava, *Miner. Eng.*, 2017, **110**, 104–121.
2 Y. Yang, S. Li, Q. Zhang, Y. Zhang and S. Xu, *Ind. Eng. Chem. Res.*, 2017, **56**, 175–182.
3 S. Martinet, in *Nanomaterials for Sustainable Energy*, ed. Q. Li, 2016, pp. 471–512.
4 N. E. F. Bloomberg, *Electric Vehicle Outlook 2023*, 2023.
5 IEA, *Global EV Outlook 2024*, 2024.
6 J. B. Goodenough and Y. Kim, *Chem. Mater.*, 2010, **22**, 587–603.
7 X. Wang, G. Gaustad, C. W. Babbitt and K. Richa, *Resour., Conserv. Recycl.*, 2014, **83**, 53–62.
8 M. Bhar, S. Ghosh, S. Krishnamurthy, Y. Kaliprasad and S. K. Martha, *RSC Sustainability*, 2023, **1**, 1150–1167.
9 T. Or, S. W. D. Gourley, K. Kaliyappan, A. Yu and Z. Chen, *Carbon Energy*, 2020, **2**, 6–43.
10 M. Chen, J. Ma, D. L. Anderson, X. J. Luo and J. B. Goodenough, *Joule*, 2019, **3**, 2622–2646.
11 G. Harper, R. Sommerville, E. Kendrick, L. Driscoll, P. Slater, R. Stolkin, A. Walton, P. Christensen, O. Heidrich, S. Lambert, A. Abbott, K. Ryder, R. Gaines and P. Anderson, *Nature*, 2019, **575**, 75–86.

12 U.S. Geological Survey, *Mineral Commodity Summaries 2023*, U.S. Department of the Interior, 2023.
13 J. Dewulf, G. Van der Vorst, J. Denturck, H. Van Langenhove, W. Ghyoot, S. Tytgat and K. Vrancken, *Resour., Conserv. Recycl.*, 2010, **54**, 229–234.
14 European Union, *Off. J. Eur. Union*, 2023, **https://eur-lex.europa.eu/eli/reg/2023/1542/oj**.
15 A. Cornelio, A. Zanoletti, M. Scaglia, E. Galli, D. La Corte, G. Biava and E. Bontempi, *RSC Sustainability*, 2024, **2**, 2505–2514.
16 B. Makuza, Q. Tian, X. Guo, K. Chattopadhyay and D. Yu, *J. Power Sources*, 2021, **491**, 229622.
17 X. Hu, E. Mousa, Y. Tian and G. Ye, *J. Power Sources*, 2020, **483**, 228936.
18 J. Zhou, J. Ni and X. Guan, *RSC Sustainability*, 2023, **1**, 2241–2253.
19 T. Matsui, T. Hanada and M. Goto, *RSC Sustainability*, 2025, **3**, 881–889.
20 C. Liu, Y. Cao, W. Sun, T. Zhang, H. Wu, Q. Liu, Z. Rao and Y. Gu, *RSC Sustainability*, 2023, **1**, 270–281.
21 K. Davis and G. P. Demopoulos, *RSC Sustainability*, 2023, **1**, 1932–1951.
22 S. M. Shin, N. H. Kim, J. S. Sohn, D. H. Yang and Y. H. Kim, *Hydrometallurgy*, 2005, **79**, 172–181.
23 P. Meshram, B. D. Pandey and T. R. Mankhand, *Hydrometallurgy*, 2014, **150**, 192–208.
24 Y. Yao, M. Zhu, Z. Zhao, B. Tong, Y. Fan and Z. Hua, *ACS Sustainable Chem. Eng.*, 2018, **6**, 13611–13627.
25 L. Gaines, Q. Dai, J. T. Vaughey and S. Gillard, *Recycling*, 2021, **6**, 31.
26 S. Sloop, L. Liu, M. Dunlap, J. Wang and H. Zhang, *Sustainable Mater. Technol.*, 2020, **25**, e00152.
27 H. Zhou, X. Zhao, C. Yin and J. Li, *Electrochim. Acta*, 2018, **291**, 142–150.
28 F. Wu, L. Li, L. Crandon, Y. Cao, F. Cheng, A. Hicks, E. Y. Zeng and J. You, *J. Cleaner Prod.*, 2022, **339**, 130697.
29 T. Yingnakorn, J. Hartley, J. S. Terreblanche, C. Lei, W. M. Dose and A. P. Abbott, *RSC Sustainability*, 2023, **1**, 2341–2349.
30 R. Madge, A. Jarvis, W. Lima da Silva, L. L. Driscoll, P. A. Anderson and P. R. Slater, *RSC Sustainability*, 2024, **2**, 1408–1417.
31 E. C. Giles, A. Jarvis, A. T. Sargent, P. A. Anderson, P. K. Allan and P. R. Slater, *RSC Sustainability*, 2024, **2**, 3014–3021.
32 C. Lei, K. S. Ryder, A. P. Abbott and J. M. Yang, *RSC Sustainability*, 2025, **3**, 1516–1523.
33 X. Wei, Z. Guo, Y. Zhao, Y. Sun, A. Hankin and M. Titirici, *RSC Sustainability*, 2025, **3**, 264–274.
34 P. Cattaneo, F. D'Aprile, V. Kapelyushko, P. Mustarelli and E. Quartarone, *RSC Sustainability*, 2024, **2**, 1692–1707.
35 J. Peng, S. Maslek and N. Sharma, *RSC Sustainability*, 2024, **2**, 1418–1430.
36 K. Gu, J. Chang, X. Mao, H. Zeng, W. Qin and J. Han, *J. Cleaner Prod.*, 2022, **369**, 133270.
37 X. Zeng and J. Li, *J. Hazard. Mater.*, 2014, **271**, 50–56.
38 L.-P. He, S.-Y. Sun, X.-F. Song and J.-G. Yu, *Waste Manag.*, 2015, **46**, 523–528.
39 Y. Zhang, Y. He, L. Ge, R. Fu, X. Zhang and Y. Huang, *J. Power Sources*, 2013, **240**, 766–771.
40 C. Tokoro, S. Lim, K. Teruya, M. Kondo, K. Mochidzuki, T. Namihira and Y. Kikuchi, *Waste Manag.*, 2021, **125**, 58–66.
41 S. Lim, K. Teruya, F. Mizumoto, M. Asao, T. Koita, T. Namihira and C. Tokoro, *IEEE Trans. Plasma Sci.*, 2022, **50**, 3625–3634.
42 M. Nakahara, T. Koita, S. Higuchi, K. Teruya, K. Shishino, K. Teshima, T. Namihira and C. Tokoro, *IEEE Trans. Plasma Sci.*, 2025, **53**(4), 678–687, in press.
43 K. Teruya, S. Lim, K. Mochidzuki, T. Koita, F. Mizumoto, M. Asao, T. Namihira and C. Tokoro, *Int. J. Plasma Environ. Sci. Technol.*, 2022, **16**, e01003.
44 T. Koita, Y. Imaizumi, A. Narita, Y. Takaya, Y. Kita, H. Akashi, T. Namihira and C. Tokoro, *Waste Manag.*, 2025, **198**, 46–54.
45 Y. Kikuchi, I. Suwa, A. Heiho, Y. Dou, S. Lim, T. Namihira, K. Mochidzuki, T. Koita and C. Tokoro, *Waste Manag.*, 2021, **132**, 86–95.
46 C. Tokoro, T. Kurihara, A. Narita and T. Koita, *J. Mater. Cycles Waste Manag.*, 2025, **27**, 2723–2735.
47 C. Tokoro, M. Nakahara, T. Koita and N. Tsuji, *Waste Manag.*, 2025, **204**, 114958.
48 National Astronomical Observatory of Japan, *Chronological Scientific Tables*, Maruzen, 2023.
49 S. Yasuhara, S. Yasui, T. Teranishi, Y. Yoshikawa, T. Taniyama and M. Itoh, *J. Power Sources*, 2019, **441**, 227194.
50 J. C. Hestenes, J. T. Sadowski, R. May and L. E. Marbella, *ACS Mater. Au*, 2023, **3**, 88–101.
51 *Thermophysical Properties Handbook*, ed. Japan Society of Thermophysical Properties, Yokendo, Tokyo, 2008.
52 J. Y. Han and S. Jung, *Batteries*, 2022, **8**, 61.
53 E. W. C. Spotte-Smith, T. B. Petrocelli, H. D. Patel, S. M. Blau and K. A. Persson, *ACS Energy Lett.*, 2023, **8**, 347–355.
54 W. Li and B. L. Lucht, *J. Electrochem. Soc.*, 2006, **153**, A1617–A1625.
55 M. Garcia, G. Nagasubramanian, D. R. Tallant and E. P. Roth, *Instability of Polyvinylidene Fluoride-Based Polymeric Binder in Lithium-Ion Cells: Final Report*, Sandia National Laboratories, Albuquerque and Livermore, SAND99-1164, 1999, DOI: **10.2172/7020**.
56 D. Leanza, C. A. F. Vaz, P. Novák and M. El Kazzi, *Helv. Chim. Acta*, 2021, **104**, e2000183.
57 M. Wang, Q. Tan, L. Liu and J. Li, *ACS Sustain. Chem. Eng.*, 2019, **7**, 12799–12806.
58 H. Akiyama and M. Akiyama, *IEEJ Trans. Electr. Electron. Eng.*, 2021, **16**, 6–14.
59 W. Diono, S. Machmudah, H. Kanda, Y. Zhao and M. Goto, *Plasma*, 2021, **4**, 309–331.